Impact of proton irradiation on photoluminescent properties of C-doped ZrO$_2$ films prepared by ALD

Anna Sytchkova [a,*], Maria Lucia Protopapa [b,**], Hristo Kolev [c], Emiliano Burresi [b], Paolo Olivero [d], Toni Dunatov [e], Zdravko Siketić [e], Leander Tapfer [b], Zhihao Wang [f,g], Hongbo He [f,h], Yanzhi Wang [f]

[a] Optical Coatings Group, Department for Energy Technologies and Renewable Sources, ENEA C.R. Casaccia, via Anguillarese 301, Rome, 00123, Italy
[b] Department for Sustainability, ENEA C.R. Brindisi, SS 7 Appia Km 706, 72100, Brindisi, Italy
[c] Institute of Catalysis, Bulgarian Academy of Sciences, Acad. G. Bonchev St., Bldg. 11, 1113, Sofia, Bulgaria
[d] Physics Department and "NIS" inter-departmental centre, University of Torino, via P. Giuria 1, 10125, Torino, Italy
[e] Laboratory for ion beam interaction, Institut Ruđer Bošković, Bijenička cesta 54, 10000, Zagreb, Croatia
[f] Laboratory of Thin Film Optics, Shanghai Institute of Optics and Fine Mechanics, No. 390 Qinghe Road, Jiading District, Shanghai, 201800, China
[g] Center of Materials Science and Optoelectronics Engineering, University of Chinese Academy of Sciences, Beijing, 100049, China
[h] Key Laboratory of Materials for High Power Laser, Shanghai Institute of Optics and Fine Mechanics, No. 390 Qinghe Road, Jiading District, Shanghai, 201800, China

ARTICLE INFO

ABSTRACT

Amorphous C-doped zirconia thin films grown by ALD technique on fused silica substrates have high transmittance and significant photoluminescence (PL) capacity suitable for application as a transparent material to convert high energy into lower energy photons as well as an optical sensor of radiation. Due to carbon doping, zirconia films present three main PL transitions: Transition I and II at λ_{em} = 450 nm (λ_{exc} = 200 and 270 nm), related to sp^3 and sp^2 C–C bonds, and Transition III at λ_{em} = 450 nm (λ_{exc} = 300 nm) that can be assigned to C=O bonds which introduce n levels in the π- π* gap. Protons with energy of 100 keV and two values of fluence ($1\bullet10^{12}$ p$^+$/cm^2 and $5\bullet10^{14}$ p$^+$/cm^2) were used to modify the film properties. The changes induced by the radiation in the chemical composition of the films have been monitored as a function of irradiation dose using in-depth resolved XPS analysis which evidenced modification of C–Zr, Zr–O, C–H, C–C/C=C and C=O bonds. We demonstrate that C–Zr bonds formed in the film depth are cleaved by protonation in favor of Zr–O, C–H and C=O bonds establishment. As a consequence, more defect levels are formed in the π- π* gap of carbon. Consequently, the emission due to Transitions III becomes more intense for high energy doses, getting intensity values close to Transitions I/II.

1. Introduction

Zirconium oxide (or zirconia, ZrO$_2$) manufactured using the atomic layer deposition (ALD) technique is a relatively uncommon thin film material for optical applications. ALD enables conformal coating of complicated surfaces and allows for atomic-scale engineering of materials and therefore, for an ideal process for engineering of the optical properties of coatings [1].

For many applications, zirconia may be implemented in the form of coatings, which may be a single film or a multilayer. Zirconia-based coatings are widely used for electric insulation in semiconductor devices [2], or as thermal barriers [3]. Zirconia thin films also represent a way to nanosize the material, which may result in an advantageous strategy for many demanding applications where traditionally bulk or powder materials have been used. The optical properties of thin films are known to be conditioned by their structure and microstructure, both dependent on the manufacturing method and the deposition conditions. Common ways to manufacture thin films of zirconia are (magnetron) sputtering [4] and electron-beam evaporation [5], although pulsed laser deposition [6] and sol-gel technique [7] may also be implemented.
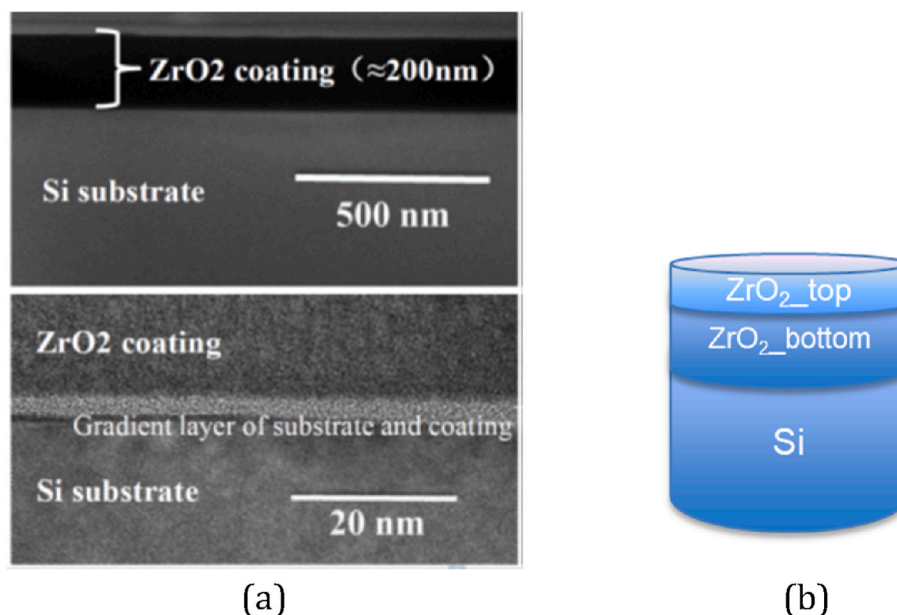
Fig. 1. Cross-section TEM image of zirconia film deposited on silicon substrate (a). Enlarged TEM image showing the microstructure of the interface gradient layer between zirconia coating and silicon substrate (b). Schematic representation of the zirconia film modeled as a bilayer of an optically denser bottom layer and a less dense top (upper) layer (c).

When starting from a metallic target, zirconia may be obtained by either post-deposition thermal annealing of sputtered zirconium, or by adding oxygen to the working gas during the deposition (reactive sputtering). Any of the aforementioned deposition techniques can provide polycrystalline or amorphous zirconia films of various packing densities and optical properties. In Ref. [8] ultrathin (about 3 nm thick) zirconia films prepared by Atomic Layer Deposition (ALD) were studied as a novel high-k material for use in microelectronics. The films were investigated for stoichiometry and surface roughness with the main focus on their electrical characteristics.

Zirconia's remarkable catalytic properties [9] and chemical persistence are exploited in bio- and medical applications [10], and it is a promising solid electrolyte [11]. The particular combination of chemical, mechanical and optical properties characterizing this ceramic renders it quite unique for applications in particularly demanding fields like technologies for space and for nuclear energy [12]. For zirconium alloys used in corrosive and nuclear environments, zirconia is a protecting layer as it is exceptionally tolerant to radiation damage [13]. It is used in radiation dosimeters and devices for radiation imaging [14].

Among the properties of zirconia readily exploitable in optics are its high refractive index and significant luminescent yield [15]. Zirconia has three crystalline phases and both crystalline and amorphous zirconia coatings may be fabricated for specific applications. Stabilization and tuning of structural and hence mechanical and optical properties of zirconia is often used by doping with metals like Ce [16] and Er [17], or other ceramics like Y_2O_3 [18], CeO_2 [19], Fe_2O_3 and MnO_2 [20]. In particular, doping may be used to tune the luminescence properties of zirconia [21,22].

Here we present a study on a set of C-doped amorphous thin films of zirconia manufactured by ALD for space applications. The films were prepared on fused silica substrates with a thickness of about 200 nm, which is relevant for many optical devices. Our recent study [23] reported characterization of these films in terms of their complex refractive index and its in-depth variation prior to and after irradiation with 100 keV protons.

This article reports on the composition and the photo-induced luminescence (PL) ability of C-doped a-ZrO_2 films. The origins of PL in zirconia is still a subject of debate [24–26]. Oxygen vacancies [27] as well as impurities, which are either deposition-dependent or absorbed upon exposure of the film to the environment [28,29], are normally indicated as PL origins. It is also known that the PL of zirconia is affected by both temperature regime and energetic particle irradiation [25]. In this study we show that the pivotal mechanism of the PL in our C-doped a-ZrO_2 films is the interaction of carbon impurities and protons with over-stoichiometric oxygen and this mechanism may be influenced by low-energy protons. Modification of the PL of the films may find applications in dosimetry and radiation imaging.

2. Experimental details

2.1. Sample manufacturing and irradiation

Zirconia films were deposited using an R-200 Advanced system by Picosun Oy, on 3 mm thick fused silica and 0.5 mm thick crystalline silicon substrates. The deposition for 2000 cycles was performed using Tetrakis zirconium $C_8H_{24}N_4Zr$ as precursor (99.999% purity, Xin-JiaYuan Chemical Technology Co., LTD, Suzhou, China) at 700 Pa pressure and the substrate temperature of 150 °C. Oxygen plasma was used as an oxidizing agent and nitrogen was filled throughout the deposition to remove excess of reactants. The chosen deposition conditions assured a relevant carbon doping level via a slightly incomplete chemical reaction towards the sample surface. As carbon doping on zirconia was obtained through incomplete chemical reaction at the last stage of the film growth, the film resulted inhomogeneous in its upper 5% of thickness, approximately. TEM analysis performed using a FEI Talos F200 (Thermo Fisher) microscope confirmed the amorphous structure of the coatings and revealed no carbon agglomerates in the films, Fig. 1a. Notice that the gradient layer between the Si substrate and the film evidenced in the figure, is composed mostly of the native silicon oxide covered with first atomic strata of zirconia. The results of ellipsometric and X-ray reflectometry analyses [23,30] revealed the in-depth inhomogeneity of the film material. All films can be modeled as bilayers, Fig. 1b, being the part near the substrate optically denser. The relatively thin upper part of all films (about 10 nm) has a lower refractive index and a higher extinction coefficient due to a higher amount of residual organic impurities.

The samples deposited on fused silica were organized in two groups which differed by the amount of the residual organic substance in the

Table 1
Irradiation parameters for the investigated samples.

Sample	Fluence (p$^+$/cm^2)	Average rate (p$^+$/cm^2 s)
7A	1,00E+12	1,67E+10
10A	1,00E+12	1,67E+10
8A	2,00E+13	1,08E+10
11A	2,00E+13	1,04E+10
11B	4,50E+12	1,08E+10
9A	5,00E+14	1,12E+11
12A	5,00E+14	2,04E+10
FS A	1,00E+12	1,71E+10
FS B	5,00E+14	6,81E+10

upper part of the film: the samples 7A, 8A and 9A were richer in doping material in their thicker upper layer, while the samples 10A, 11A and 12A had thinner upper layer with less doping [30].

The samples were then irradiated by low-energy protons (100 keV) at fluence ranging from $1\bullet10^{12}$ p$^+$/cm^2 through $5\bullet10^{14}$ p$^+$/cm^2, Table 1, repeating the irradiation conditions for each of two groups of samples. The irradiation was conducted at the DiFU beamline of the Laboratory for ion beam interactions, RBI. A 100 keV proton beam was obtained using the 1 MV electrostatic Tandetron accelerator with a terminal voltage of 50 kV. Prior to irradiation, the chamber was evacuated down to $5\bullet10^{-6}$ - $5\bullet10^{-7}$ mbar. The beam was scanned over the sample using electrostatic scanners in order to homogenize the dose, and the current was monitored with periodic Faraday cup insertions, as well as readings from slits touching the outside of the beam. The area scanned is defined by the slits and was set to 1×1.5 cm^2, and 1.5 x.1.5 cm^2, depending on the sample.

2.2. Characterization techniques

Optical, microstructural and compositional properties of the C-doped zirconia samples have been thoroughly investigated before and after proton irradiation and reported in our previous publication [23].

X-ray photoelectron measurements were conducted using the K-Alpha electron spectrometer from Thermo Fisher Scientific, featuring an analysis chamber with a base pressure better than 10^{-9} Torr. The spectrometer is equipped with a twin anode MgKα/AlKα monochromated X-ray source with excitation energies of 1253.6 and 1486.6 eV, respectively. For the measurements, the AlKα monochromated X-ray source (1486.6 eV) was utilized, employing a 400 μm beam spot. A low-energy electron beam and a low-energy ion beam were employed to neutralize the charge on the surface of the insulating sample. The instrumental resolution is better than 0.5 eV, measured as the full width at half maximum (FWHM) of the Ag3d$_{5/2}$ photoelectron peak. The measurements were conducted using an analyzer pass energy of 50 eV. To obtain accurate information about composition and chemical states while mitigating the influence of water vapor and contaminants on the film surface in ambient air, a 1 keV Ar$^+$ ion etching process for 80 s preceded the XPS measurement. CasaXPS software (Casa Software Ltd) was employed for data analysis. The spectral processing involved the subtraction of a Shirley-type background [31]. Peak positions and areas were determined through symmetrical Gaussian-Lorentzian curve fitting. For calculation of the correct posion of the C1s peak, the literature value reporting a work function FSA of 4.76 eV for atomic layer deposited ZrO$_2$ coated samples was used [32]. The corrected C1s peak position is then E$_B$ = 289.58 eV – FSA = 284.82 eV. Relative concentrations of different chemical species were derived by normalizing peak areas to their photoionization cross-sections, calculated using the Scofield method [33].

The chemical composition analysis encompassed both the film surface and an in-depth profile. XPS measurements were carried out focusing on the C1s, O1s, and Zr3d core levels at three distinct depths within the film. These depths were obtained after sputtering with Ar$^+$ ions for durations of 600 s, 1200 s, and 1740 s, respectively. These
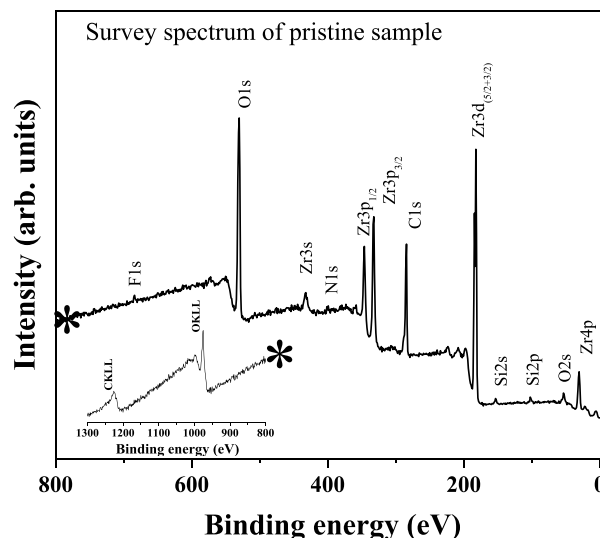

Fig. 2. XP Survey spectrum/spectra of the pristine and sputtered sample of C-doped ZrO$_2$ films prepared by ALD. An asterisk (*) is used to denote the point where the spectrum is interrupted. The energy range between 800 and 1300 eV is displayed in the embedded figure to showcase the complete spectrum with maximum visibility.

sputtering times roughly correspond to depths of 60 nm, 120 nm, and 170 nm from the surface, covering approximately 1/3, 2/3, and almost the entire thickness of the film.

Photo-induced luminescence was measured by a FluoroMax 4 spectrofluorometer (Horiba Jobin Yvon, Edison, NJ, USA). Adjustment of the position of the sample was necessary in order to get an incidence angle of 30°.

3. Characterization results and discussion

3.1. XPS analysis

X-ray photoelectron spectroscopy was employed to explore both the surface and in-depth profile of the zirconia film deposited on a silicon substrate. Utilizing XPS data, we extracted insights into the oxidation states and atomic concentrations of the surface elements. This allowed us to delineate the evolution of the film along its thickness and evaluate the influence of protonation on C-doped zirconia films.

Fig. 2 displays the survey spectra of the pristine sample as initially prepared and introduced into the vacuum chamber. To avoid the influence of surface-adsorbed contamination, the XPS analyses were carried out after surface etching for 80 s. The data obtained reveal core level peaks of elements, including zirconium (Zr3d), oxygen (O1s), and carbon (C1s), which constitute the film. Additionally, minor contaminations such as fluorine (F1s core level), likely originating from the scroll pump, along with traces of nitrogen and silicon, are also observed.

Survey spectra are commonly employed to identify elements, and more detailed information can be gleaned through high-resolution XP spectra, as illustrated in Fig. 3. In Fig. 3a, high-resolution XP spectra of the Zr3d core level are presented, measured on the pristine ZrO$_2$ sample (top) and during depth profiling with three different Ar$^+$ ion exposures (from top to bottom 600 s, 1200 s, and 1800 s, respectively).

The measured Zr–O binding energy (BE) at the surface of the pristine sample is 181.9 eV, exhibiting a slight deviation of approximately 0.5 eV from the value of 182.4 eV reported in Ref. [34]. Comparable BE have been reported for the surfaces of monoclinic ZrO$_2$ films (181.6 eV) [35], which is even 0.3 eV lower compared to the BE defined in our case. This discrepancy of approximately 0.5 eV can be elucidated by the electrostatic potential built up at the interface between different materials,
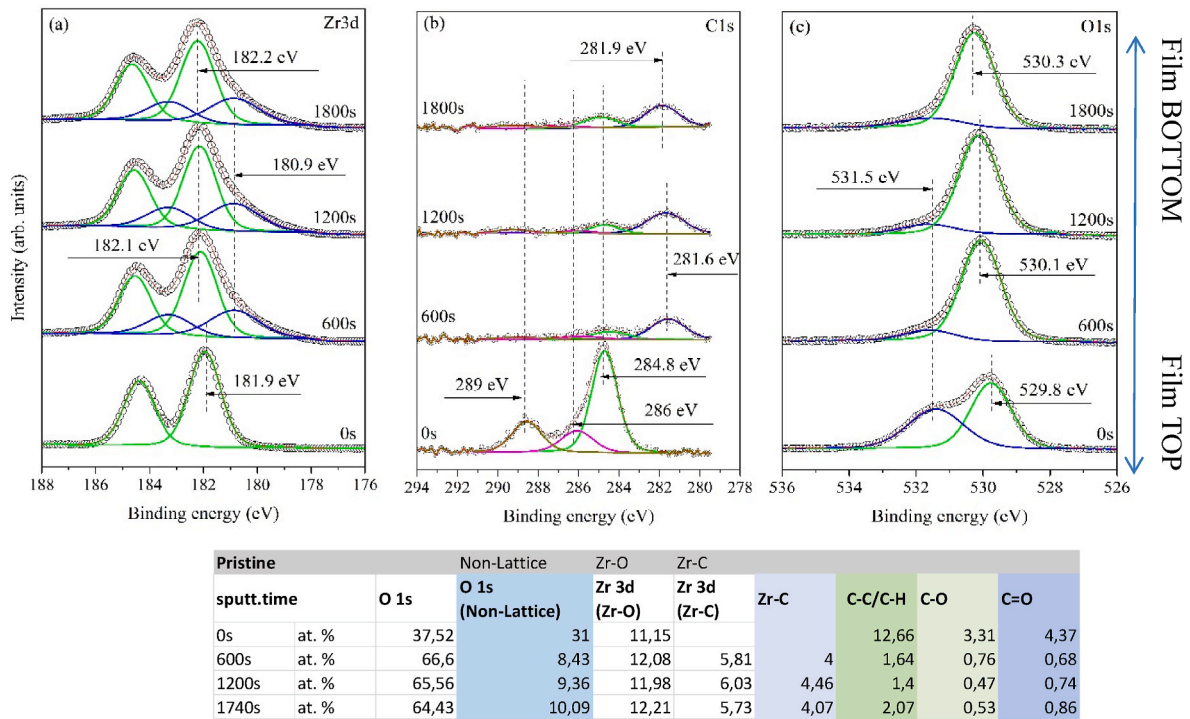
Pristine			Non-Lattice	Zr-O	Zr-C				
sputt.time		O 1s	O 1s (Non-Lattice)	Zr 3d (Zr-O)	Zr 3d (Zr-C)	Zr-C	C-C/C-H	C-O	C=O
0s	at. %	37,52	31	11,15			12,66	3,31	4,37
600s	at. %	66,6	8,43	12,08	5,81	4	1,64	0,76	0,68
1200s	at. %	65,56	9,36	11,98	6,03	4,46	1,4	0,47	0,74
1740s	at. %	64,43	10,09	12,21	5,73	4,07	2,07	0,53	0,86

Fig. 3. Evolution of the high-resolution XP spectra of core levels of Zr3d (a), C1s (b) and O1s (c) along the thickness of a pristine ZrO_2 film.

tending to align the Fermi levels. Similar effects have been reported for ZrO_2 clusters in contact with NiO substrates [36]. The inhomogeneity of our films having top sub-layer richer in organic residuals, Fig. 1, can be hence the reason of such a discrepancy.

Moving to in-depth profiling, two major differences in the Zr3d spectrum are observed. The line shape of the spectra changes, indicating the presence of two oxidation states of zirconium. Based on the curve-fitting procedure, a doublet peak is obtained with a BE of 182.1–182.2, attributed to a large part of the maximum coordination zirconium (Zr^{4+}) in Zr–O bonding (peaks colored in green), and another peak with a BE of 180.9 eV is ascribed to the presence of Zr–C bonding (peaks colored in blue) [37]. Due to the lower electronegativity of carbon compared to oxygen, the $Zr3d_{5/2}$ core level binding energy is lower for zirconium atoms bonded to carbon atoms than for zirconium atoms bonded to oxygen. For each analyzed sample, no sub-oxides compounds like Zr_2O_3 and ZrO were detected. This indicates that ZrO_2 is the predominant oxidized species [38], as evident from the surface atomic concentrations shown in the table below the spectra in Fig. 3. The difference in BE energy between the pristine and sputtered surfaces can be explained by changes in the electrostatic potential between zirconia and silicon layers after sputtering the surface with the positive charge of Ar^+ ions, revealing the mixture between zirconia and zirconium carbide in the film.

Confirmation of the presence of zirconium carbide in the film is provided by the Zr–C bond signal evident in the C1s core level band acquired at internal film levels, as illustrated in Fig. 3b (peaks marked in blue) [39]. Alongside the Zr–C bond, three additional components were utilized to fit the high-resolution XP spectra of the C1s core level. The first component corresponds to the carbonate bond C=O, with a binding energy (BE) of approximately 289 eV (peaks marked in purple). The second component corresponds to the C–O bond with a BE of around 286 eV (peaks marked in orange). The third component corresponds to the C–C/C–H bonds, possessing a BE of 284.8 eV (peaks marked in green), typically attributed to adventitious hydrocarbons on the surface. These hydrocarbons were easily removed during the film sputtering, as evidenced by the atomic concentration calculations presented in the table below the spectra in Fig. 3. Numerous scientific papers report the BE of different bonds between carbon-carbon and carbon-oxygen. As a reference, the work by G. Greczynski and L. Hultman [40] can be cited. For the C1s core level at the top of the film, only three contributions were employed for fitting, as the Zr–C bond signal was absent in that spectrum, supporting the earlier analysis of the Zr3d core level. Additionally, considering the atomic concentrations (table below the spectra in Fig. 3), it is observed that the ratio between the zirconium and carbon contents, ascribed to zirconium carbide after the curve-fitting procedure, closely aligns with the theoretically expected Zr:C ratio of 1:1. In our case, we calculated Zr:C to be approximately (4.0–4.5): (5.7–6.0). The slight deviation from the theoretical ratio can be attributed to errors introduced by the curve-fitting procedure and the noisy spectrum of the C1s core level, leading to inaccuracies in peak area estimation used for concentration calculations.

Fig. 3c) illustrates the progression of the O1s core level for the pristine sample and three in-depth surfaces (600 s, 1200 s, and 1800 s) from top to bottom, respectively. The curve fitting procedure reveals two main contributions. We opted for a streamlined curve fitting procedure with a minimal number of peaks, as a more intricate fitting with additional peaks doesn't significantly contribute to the film analysis. The primary contribution, depicted by the green peak in Fig. 3c), is attributed to the Zr–O bond with a measured binding energy (BE) of core level of 529.8 eV for the pristine surface and 530.1–530.3 eV for surfaces measured after Ar^+ ion etching. As anticipated, we observe a shift of approximately 0.4 eV in the BE compared to literature data [33]. Once

Table 2
XPS binding energies (BEs) of the pristine sample and the in-depth surfaces.

	0s	600s	1200s	1800s
C–Zr	–	281.6	281.7	281.9
C–C	284.7	284.5	284.7	284.9
C–O	286.1	285.8	286.0	286.6
C=O	288.6	288.9	289.3	289.3
Zr–O	529.8	530.1	530.1	530.3
OH/COx	531.4	531.6	531.6	531.6
Zr–O	181.9	182.1	182.1	182.2
Zr–C	–	180.9	180.9	180.9

Sample 7A

sputt.time		O 1s	O 1s (Non-Lattice)	Zr 3d (Zr-O)	Zr 3d (Zr-C)	Zr-C	C-C/C-H	C-O	C=O
			Non-Lattice	Zr-O	Zr-C				
600s	at. %	65,11	10,05	12,64	4,92	3,53	1,76	0,86	1,13
1200s	at. %	67,32	9,27	12,07	5,46	3,33	1,49	0,76	0,29
1740s	at. %	67,91	8,2	12,14	5,3	3,88	1,46	0,78	0,33

Sample 10A

sputt.time		O 1s	O 1s (Non-Lattice)	Zr 3d (Zr-O)	Zr 3d (Zr-C)	Zr-C	C-C/C-H	C-O	C=O
			Non-Lattice	Zr-O	Zr-C				
600s	at. %	66,99	8,44	12,12	5,31	3,71	1,91	0,56	0,96
1200s	at. %	66,27	9,51	11,48	5,58	3,32	2,29	0,81	0,74

Sample 9A

sputt.time		O 1s	O 1s (Non-Lattice)	Zr 3d (Zr-O)	Zr 3d (Zr-C)	Zr-C	C-C/C-H	C-O	C=O
			Non-Lattice	Zr-O	Zr-C				
600s	at. %	65,1	11,54	11,94	5,16	3,1	1,79	0,67	0,69
1200s	at. %	64,51	12,84	11,56	5,29	2,54	1,88	0,64	0,75
1740s	at. %	67,02	10,52	11,62	5,36	2,51	1,86	0,54	0,58

Sample 12A

sputt.time		O 1s	O 1s (Non-Lattice)	Zr 3d (Zr-O)	Zr 3d (Zr-C)	Zr-C	C-C/C-H	C-O	C=O
			Non-Lattice	Zr-O	Zr-C				
600s	at. %	67,18	8,76	11,73	5,61	3,64	1,47	0,84	0,77
1200s	at. %	66,78	9,15	12,04	5,19	3,42	2,32	0,37	0,74
1740s	at. %	67,32	8,08	11,66	5,51	4,07	1,8	0,69	0,87

Fig. 4. Evolution of the principle XPS core levels for carbon, oxygen and zirconium along the thickness of irradiated C-doped ZrO_2 films.
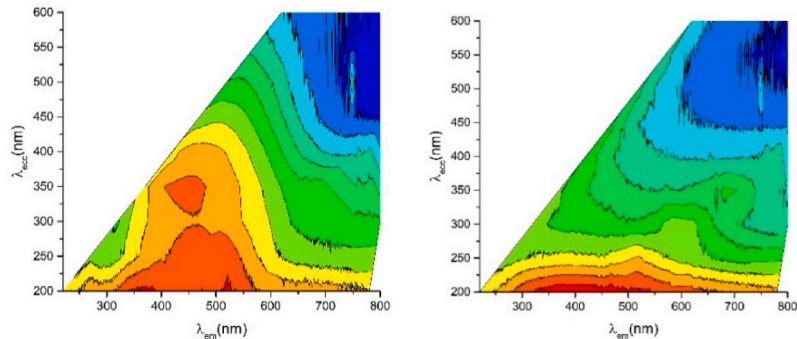

Fig. 5. PL maps for a pristine ZrO_2 film on fused silica (left) and on a bare fused silica substrate (right). The excitation wavelengths and the corresponding emission wavelengths are given on the y and x-axes, respectively.

again, the electrostatic potential within the zirconia film accounts for this discrepancy, which nearly vanishes after sputtering.

The higher BE peak, indicated by the blue line in Fig. 3c) and labeled as non-lattice oxygen in the table below the spectra in Fig. 3, comprises at least two possible peaks attributed to surface groups of OH/CO_X [33]. Oxygen vacancies in this energy range are unlikely, as they stabilize the tetragonal zirconia film and induce n-doping via filled gap states, leading to shifts towards higher BE [34]. These volatile species are weakly bonded, and the decrease in this peak may be partially attributed to the sputtering performed for the in-depth analysis.

The precise binding energies (BEs) of the pristine sample and the in-depth surfaces are consolidated in Table 2, enabling the tracking of BE evolution attributed to alterations in the electrostatic potential at various depths of the C-doped ZrO_2 films following Ar^+ ion sputtering.

After the proton irradiation, for all our samples, a general decrease of the ratio of the Zr–C peaks (both intensity and area), with respect to the other peaks within the same core level energy range, was observed, Fig. 4. This means that the ratio Zr–C/Zr–O intensity decreased upon irradiation. The ratios between Zr–C and the other bonds C–C/C–H, C–O and C=O intensities decrease with irradiation as well. In particular, this effect is more evident for samples 9A and 12A (fluence of $5 \bullet 10^{14}$ p^+/cm^2), along the entire film thickness but especially at the film bottom, whereas this ratio is slightly lower for the samples irradiated at lower dose (7A and 10A, fluence $1 \bullet 10^{12}$ p^+/cm^2). In particular, for sample 7A and 10A, protonation induced an increase of the C–C/C–H signal with respect to Zr–C exclusively at the top layer of the film, i.e. at 1/3 of the film thickness (60 nm). Conversely, for the samples 7 and 9 with initially higher amounts of non-lattice oxygen (higher O–H bond signal in O1s core level and C–O bond in C1s core level) this signal further increases upon irradiation and is further homogenized along all the film thickness with the dose increase. This effect is much less expressed for the samples 10A and 12A with initially lower content of non-lattice oxygen. Therefore, we infer that protonation induces cleavage of Zr–C bonds. Depending on the sample C-doping level (connected to the initial amount of non-lattice oxygen), this cleavage may induce formation of C=O and C–C/C–H bonds as well as liberation of electrically neutral carbon atoms further dissolved in the zirconia matrix. The homogenization of the signal related to these bonds is determined by the increase
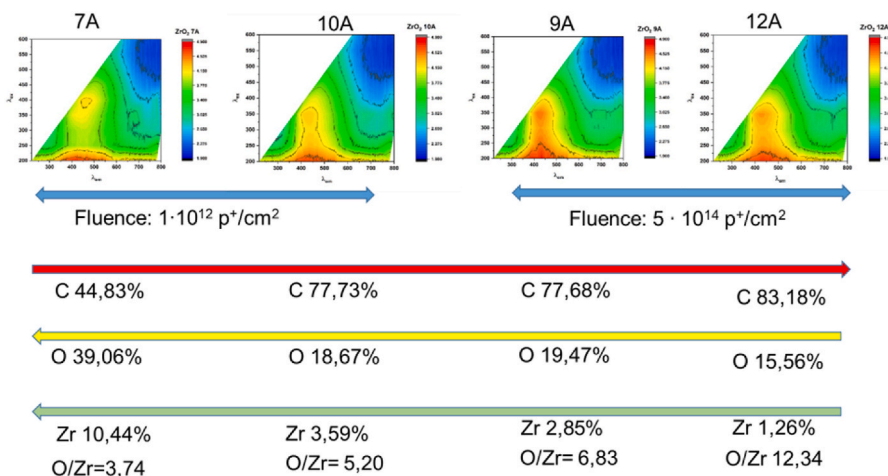

Fig. 6. PL maps for irradiated ZrO_2 films. Modification of the content of carbon, oxygen and zirconium on the films surface due to irradiation.

Table 3
Parameters adopted in the SRIM simulation of 100 keV proton irradiation in C-doped ZrO_2.

Atom	Zr	O	C
Stoichiometry	1	2	0.001
Displacement energy (eV)	25	28	28
Lattice Binding Energy (eV)	3	3	3
Surface Binding Energy (eV)	6.33	2	7.41
Mass density (g cm^{-3})	5.68		

of the irradiation effect along the distance from the sample surface, which compensates the initial inhomogeneity of the film material. Formation of carbonates, hydrocabonates and neutral interstitial carbon impurities at the expense of carbide is hence an effect of protonation of our ZrO_2 films. This effect is less pronounced for the samples initially poorer in doping material and in non-lattice oxygen.

3.2. Analysis of PL maps

Fig. 5 reports PL maps obtained for pristine zirconia sample (a) and bare fused silica substrate (b), while Fig. I in the Supporting Information (S.I.) gives PLE spectrum. The PL and PLE data show that the visible emission around 450 nm can be activated by three possible transitions as schematically illustrated in Fig. 5 of Ref. [41]: the first one (I) at higher energies (λ_{exc}~200 nm) may be ascribed to $\sigma \rightarrow \sigma^*$ excitation, the second one (II) at λ_{exc}~270 nm corresponds to the $\pi \rightarrow \pi^*$ excitation, while the third one (III) at λ_{exc}~360 nm corresponds to the $n \rightarrow \pi^*$ excitation. For all three transitions, the emission is due to radiative decay from π^* level to n defects levels inside $\pi \rightarrow \pi^*$ gap. For the transition I the radiative decay is accompanied by non-radiative decay from σ^* to π^* level.

Fig. 6 reports PL maps for irradiated samples together with the element abundance retrieved from the survey spectrum taken at the surface of the irradiated samples. The atomic percentage as a function of the etching time is given for all the irradiated samples in Fig. II of S.I (with 1200 s of etching time corresponding to a penetration depth of 120 nm). As one can note in Fig. 6, the PL intensity ratio of Transition III with respect to Transition I and II increases for the two samples irradiated at higher doses, maybe due to the higher content of carbon partially bonded to oxygen which form n-levels inside π -π^* gap. In fact, oxygen content on the surface is very high, giving a ratio with Zr content much higher than the value expected for stoichiometric zirconia (O/Zr = 2), especially for samples protonated at higher doses for whom the O/Zr ratio gets values up to 7 and 12. In particular, the ratio between C=O and C–Zr bonds is higher for the irradiated samples as compared to the pristine samples (see Figs. 3 and 4), and it increases with the dose. C=O bonds in carbon materials are known to be responsible for the emission at λ_{em} = 450 nm excited at λ_{exc} = 300 nm (Transition III) [34]. Therefore, this kind of emission is more intense for high dose-irradiated samples, most probably due to the higher abundance of C=O bonds. The carbon increases on the surface along the radiation dose is due to the build-up of a carbonaceous contamination layer during the irradiation [23]. Although very thin (determined as 0.7 nm for the highest of used fluences [23]) such a layer is sufficiently thick to influence the survey mean values as the information depth of the XPS is approximately 5–10 nm which is comparable with the thickness of the contamination layer rich in carbon.

3.3. Theoretical simulation of proton-induced damage in C-doped ZrO_2

In simulating the structural effects of proton irradiation in amorphous C-doped zirconia, the "*Detailed calculation with full damage cascades*" mode in SRIM [42] was employed, and the parameters listed in Table 3 were adopted.

It is worth remarking that the reported carbon concentration is defined on an "upper limit" basis, and even in this case the effect of
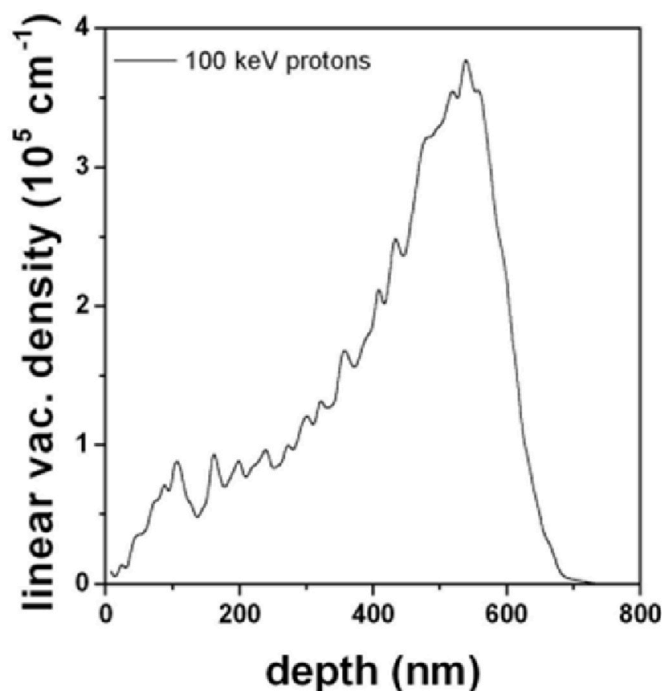
Fig. 7. Linear vacancy density profile induced by 100 keV protons in carbon-doped zirconia.

Table 4
Geometrical ion penetration features for 100 keV protons in carbon-doped zirconia.

Direction	Range (nm)	Straggle (nm)
Longitudinal	542	85
Lateral projection	88	112
Radial	138	78

carbon incorporation in the ZrO_2 matrix can be regarded as negligible in terms of the modeled depth profile of the linear density of induced vacancies. From such a profile (reported in Fig. 7) it is possible to estimate the geometrical features summarized in Table 4.

The damage density linearly increases from the film surface towards its depth. This means that the inner part of the film undergoes heavier impact from the radiation. The film material undergoes the structural transformations analyzed in the previous section. The occurrence of these effects is larger in the upper part of the film due to a higher concentration of impurities. On the other hand, the proton impact increases with the film depth. These two effects induce film densification and lead to a more uniform film. After irradiation, the upper layer rich in impurities becomes much thinner, while the rest of the film is less absorbing [30].

Notice that although, to evaluate the fractions of displaced atoms of each type, our theoretical calculations used the hypothesized stoichiometry reported in Table 3, for different concentration of dopant carbon atoms, the calculation remains valid in terms of fractions. In particular, for the fluence of $5 \bullet 10^{14}$ cm^{-2}, roughly 0.05% of the carbon atoms in the surface region are moved from their positions by protons. If the carbon doping scales by a factor in excess or in deficiency, the fraction of displaced atoms remains the same, while the volumetric density of displaced atoms scales accordingly. The "golden rule" is valid: in a "low concentration" approximation (i.e. low concentration of carbon atoms, relatively low fluence of implanted ions, low probability that a "light" proton displaces a "heavy" carbon), it is reasonable to imagine that the scaling is linear.
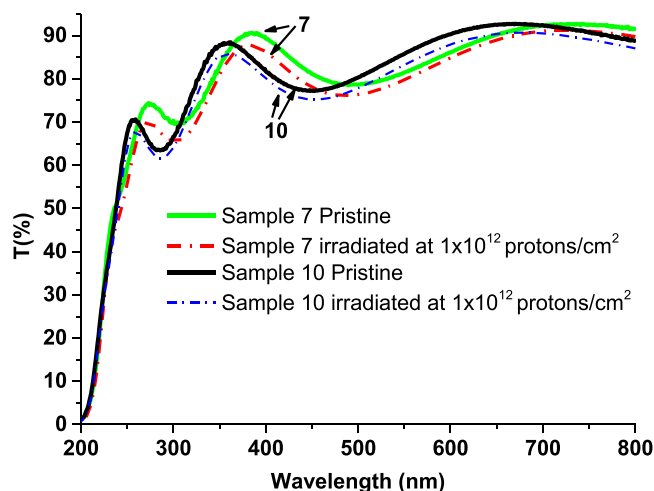
Comparison with the stoichiometry estimated from the XPS

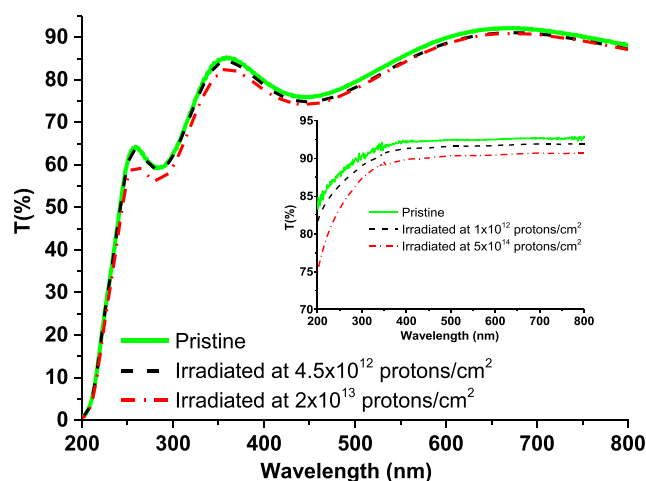**Fig. 8.** Transmittance of samples 7 and 10 before and after irradiation.

Fig. 9. Transmittance of samples 11A and 11B and of the uncoated fused silica substrate (in insert) before and after irradiation.

measurement is not straightforward. Indeed, the XPS intensity is influenced by various instrumental and physical variables, as well as by potential contaminants, making it unrealistic to expect perfect alignment with theoretical ratios Therefore retrieving of stoichiometric ratio between surface elements can be challenging. Additionally, the theoretical SRIM simulations primarily focus on bulk properties, incorporating a larger volume in comparison to the surface measurements, which typically extend only about 10 nm or even less. This natural difference between surface and bulk properties is a common phenomenon observed in experiments that involve both bulk and surface analyses. The unique characteristics of surfaces often lead to different outcomes due to their distinct structural and chemical attributes. This is a natural consequence of the inherent nature of surfaces. For these reasons here we estimate the proton impact in terms of fraction of displaced atoms starting from a hypothetical value of carbon doping.

3.4. Radiation impact on the composition of C-doped zirconia films

The change of the optical properties for the two types of films was different. Fig. 8 compares the transmittance change for the samples 7 and 10 which belong to two different sample types and were irradiated at the same conditions. The induced decrease of transmittance is smaller

for sample 10 in the entire investigated spectral range and it is nearly constant, about 2–3 %. Instead, for sample 7 the same level of transmittance decrease is observed for the range over 600 nm, while the discrepancy is significantly more pronounced towards the shorter wavelengths, exceeding 5% in the ultraviolet.

For some samples, moderate radiation doses produced either no change or even a slight increase in the sample transmittance in the ultraviolet (UV) range. Fig. 9 illustrates this effect with an example of the samples 11A and 11B which belong to the same group as sample 10. For the sample 11B which received a dose of 4.5×10^{12} p$^+$/cm^2, the transmittance curve overlaps with that of the pristine sample in the range below 400 nm. For comparison, the insert in Fig. 9 reports the measured spectral transmittance for the uncoated fused silica substrate, for two different irradiation conditions. In the case of fused silica substrate, the damage reduction of the transmittance is well known [43]. For the substrate, the transmittance decrease is present in the entire spectral range and, with the radiation dose increased, the transmittance decay is increasing and more pronounced at shorter wavelengths.

As illustrated in the previous section, the substrates are more affected by the damage induced by 100 keV protons, Fig. 7. A fused silica substrate irradiated at the same conditions used for sample 11B loses about 2% of its transmittance due to formation of a ~600 nm-thick damaged zone inside the material. This transparency lost is spectrally nearly uniform for the range 200–800 nm. The same value of the transparency decay is kept for sample 11B in the visible and infrared range, while no transmittance decrease occurs in the UV for this sample, as illustrated in Fig. 9. Therefore, the unchanged UV-transmittance of sample 11B proves a significant enlargement of the UV transparency of the film materials. In fact, the induced modification within ~190 nm of the film has been sufficient to compensate the decrease of the substrate transparency due to the 600 nm-thick absorbing zone formed beneath the substrate surface.

The transparency increase in C-doped zirconia films can be explained by reduction of carbon-related absorption. Indeed, thin films of amorphous carbon have a broad band absorption which maximum is positioned in the spectral range of carbon interband transitions 250–350 nm, as illustrated by Fig. 3 in Ref. [45]. These transitions have sp^3 (diamond-like) and sp^2 (graphite-like) characters, but mostly the absorption is determined by strong σ→σ* transitions [47].

Indeed, we have demonstrated here that the proton irradiation produced cleavage of Zr–C bonds leading to formation, in particular, of carbon interstitials which are electrically neutral and hence do not absorb in the optical range of study. Additionally, during the irradiation, the film material may undergo chemical reactions similar to those happening during the ALD growth [e.g. 46] where metal-organic precursor interacts with oxygen and protons when water as co-reactant is used. Such reactions can lead to reduction of the carbon-related absorption. Notice that the non-lattice oxygen abundance in our zirconia films can act as oxidizer source for the completion of the reaction only partially completed during the film growth.

The reduced carbon-related absorption in the irradiated films was evidenced also by the reduction of the C1s-peak area in the XPS survey for the irradiated films compared to pristine ones. For the C1s-peak area estimation, the measurements acquired after etching for dozens of seconds were considered, so that the measurements were not affected by surface adsorption pollution. Thermo's Avantage software used for this calculation takes into account the sensitivity factor for each element.

The enhancement of the UV transparency of the C-doped zirconia layers due to the impact of energetic particles was confirmed for all the samples by their increased laser-damage threshold values upon proton irradiation [44].

Summarizing, we can state that the XPS depth-resolved investigations revealed the cleavage of Zr–C and of C=O bonds as well as establishment of O–H and C–O bonds (HCO species formation), both increasing towards the film bottom and as the dose increases. The carbonyl C=O species are those responsible for the PL signal (Transition
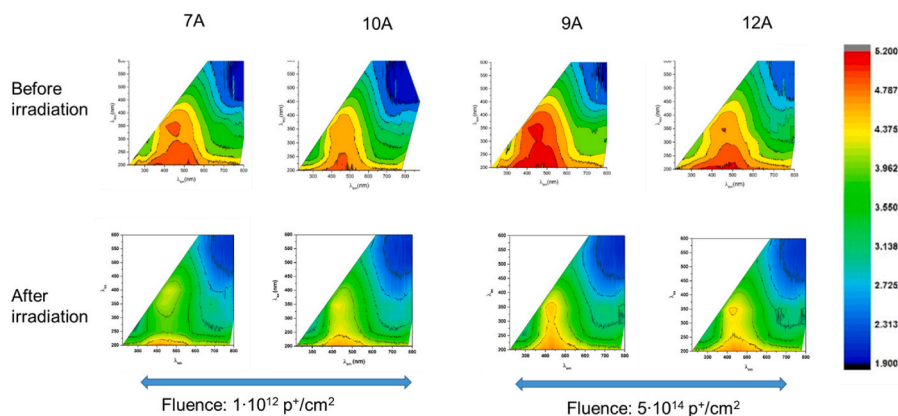
Fig. 10. PL maps for pristine (upper frame) and irradiated (lower frame) ZrO$_2$ films. Modification of the content of carbon, oxygen and zirconium in the films due to irradiation. Notice that the absolute values of intensities after irradiation were lower due to mask application during the measurement, while masking was not used for pristine samples.

II). The possibly formed C–H bonds may increase and this effect is more evident for higher radiation doses. Concerning the remaining carbon content, the percentage of carbon bonded to oxygen becomes higher for the samples irradiated at higher dose and this effect induces the increase of PL emission at $\lambda_{em} = 450$ nm excited at $\lambda_{exc} = 300$ nm (Transition II) with respect to the emission at $\lambda_{em} = 450$ nm excited at $\lambda_{exc} = 200$–270 nm (Transition I).

Fig. 10 gives a comparison between PL maps of each sample before and after irradiation and it is evident that the decrease of emission intensity for all the analyzed irradiated samples. This is due to reduction of carbon-zirconium bonds and decrease of carbon content inside the film upon the irradiation. The effect is most pronounced for sample 7A, which indeed has the lowest C=O bond in C1s core level after irradiation, Fig. 4.

4. Conclusions

Amorphous C-doped zirconia thin films obtained using ALD technique on fused silica substrates have high transmittance and significant PL capacity. Carbon doping of zirconia was obtained through incomplete chemical reaction at the last stage of film growth. Due to carbon doping, zirconia films present three main PL transitions: Transition I and II at $\lambda_{em} = 450$ nm ($\lambda_{exc} = 200$ and 270 nm), related to sp^3 and sp^2 C–C bonds, and Transition III at $\lambda_{em} = 450$ nm ($\lambda_{exc} = 300$ nm) that can be assigned to C=O bonds which introduce n levels in the π- π* gap.

Since the high transparency of the films in the visible range is preserved by limiting the carbon content, the carbon-doped zirconia may find application as a transparent material to convert high energy into lower energy photons. Moreover, thanks to the substantial change of its optical properties under irradiation, the C-doped zirconia may find application as an optical sensor of radiation. In this study we hence investigated how the PL properties in C-doped zirconia films on silica substrate change under proton radiation. The films underwent low-energy proton irradiation with energy of 100 keV and two values of proton fluences ($1 \bullet 10^{12}$ p$^+$/cm^2 and $5 \bullet 10^{14}$ p$^+$/cm^2) were used. The changes induced by the radiation in the chemical composition of the films have been monitored as a function of irradiation dose. To this aim, the in-depth resolved XPS analyses have been performed on both the pristine and irradiated samples. The ratio Zr–C/Zr–O bonds decreases under irradiation while the ratio C–H/C–Zr bonds increases, especially at higher doses. Analogously, the ratio C=O/C–Zr bonds increases with respect to pristine samples, especially for high-dose irradiated samples. Therefore, we can conclude that C–Zr bonds are cleaved by protonation in favor of Zr–O, C=C/C–C/C–H and C=O bonds establishment. As a consequence, more defect levels are formed in the π- π* gap of carbon. Consequently, the emission due to Transitions III becomes more intense

for high energy doses, getting intensity values close to Transitions I/II.

CRediT authorship contribution statement

Anna Sytchkova: Writing – review & editing, Writing – original draft, Supervision, Project administration, Methodology, Investigation, Funding acquisition, Formal analysis, Data curation, Conceptualization. **Maria Lucia Protopapa:** Writing – review & editing, Writing – original draft, Methodology, Investigation, Formal analysis, Data curation. **Hristo Kolev:** Writing – review & editing, Visualization, Investigation, Formal analysis. **Emiliano Burresi:** Writing – review & editing, Visualization, Investigation. **Paolo Olivero:** Writing – review & editing, Writing – original draft, Methodology, Formal analysis. **Toni Dunatov:** Writing – review & editing, Investigation. **Zdravko Siketić:** Investigation. **Leander Tapfer:** Writing – review & editing, Investigation. **Zhihao Wang:** Investigation, Formal analysis. **Hongbo He:** Writing – review & editing, Funding acquisition. **Yanzhi Wang:** Writing – review & editing, Project administration, Investigation.

Declaration of competing interest

The authors declare that they have no known competing financial interests or personal relationships that could have appeared to influence the work reported in this paper.

Data availability

Data will be made available on request.

Acknowledgments

Appendix A. Supplementary data

Supplementary data to this article can be found online at https://doi.

org/10.1016/j.vacuum.2024.113083.

References

[1] Z. Chen, Q. Xu, K. Zhang, W.-H. Wong, D.-L. Zhang, E.Y.-B. Pun, C. Wang, Efficient erbium-doped thin-film lithium niobate waveguide amplifiers, Opt. Lett. 46 (2021) 1161, https://doi.org/10.1364/OL.420250.

[2] G. Adamopoulos, S. Thomas, P. Wöbkenberg, D. Bradley, M. McLachlan, T. Anthopoulos, High-mobility low-voltage ZnO and Li-doped ZnO transistors based on ZrO2 high-k dielectric grown by spray pyrolysis in ambient air, Adv. Mater. 23 (2011) 1894–1898.

[3] D. Clarke, S. Phillpot, Thermal barrier coating materials, Mater. Today 8 (2005) 22–29.

[4] A. Hojabri, Structural and optical characterization of ZrO2 thin films grown on silicon and quartz substrates, J Theor Appl Phys 10 (2016) 219–224, https://doi.org/10.1007/s40094-016-0218-8.

[5] M. Jerman, Z. Qiao, D. Mergel, Refractive index of thin films of SiO2, ZrO2, and HfO2 as a function of the films' mass density, Appl. Opt. 44 (2005) 3006–3012, https://doi.org/10.1364/AO.44.003006.

[6] S. Heiroth, R. Ghisleni, T. Lippert, J. Michler, A. Wokaun, Optical and mechanical properties of amorphous and crystalline yttria-stabilized zirconia thin films prepared by pulsed laser deposition, Acta Mater. 59 (2011) 2330, https://doi.org/10.1016/j.actamat.2010.12.029.

[7] J.S. Lakshmi, I. John Berlin, G.P. Daniel, P.V. Thomas, K. Joy, Effect of calcination atmosphere on photoluminescence properties of nanocrystalline ZrO2 thin films prepared by solgel dip coating method, Phys. B Condens. Matter 406 (2011) 3050, https://doi.org/10.1016/j.physb.2011.05.004.

[8] M.A. Botzakaki, N. Xanthopoulos, E. Makarona, C. Tsamis, S. Kennou, S. Ladas, S. N. Georga, C.A. Krontiras, ALD deposited ZrO2 ultrathin layers on Si and Ge substrates: a multiple technique characterization, Microelectron. Eng. 112 (2013) 208–212, https://doi.org/10.1016/j.mee.2013.03.002.

[9] L. Song, X. Cao, L. Li, Engineering stable surface oxygen vacancies on ZrO2 by hydrogen-etching Technology: an efficient support of gold catalysts for water-gas shift reaction, ACS Appl. Mater. Interfaces 10 (2018) 31249–31259.

[10] S.J. Malode, N.P. Shetti, "ZrO2 in Biomedical Applications" in Metal Oxides for Biomedical and Biosensor Applications, 2021, pp. 471–501, https://doi.org/10.1016/B978-0-12-823033-6.00016-8.

[11] T. Liu, X. Zhang, X. Wang, et al., A review of zirconia-based solid electrolytes, Ionics 22 (2016) 2249–2262, https://doi.org/10.1007/s11581-016-1880-1.

[12] P. Kalita, S. Ghosh, G. Gutierrez, et al., Grain size effect on the radiation damage tolerance of cubic zirconia against simultaneous low and high energy heavy ions: nano triumphs bulk, Sci. Rep. 11 (2021) 10886, https://doi.org/10.1038/s41598-021-90214-6.

[13] K.E. Sickafus, Hj Matzke, Th Hartmann, K. Yasuda, J.A. Valdez, P. Chodak, M. Nastasi, R.A. Verrall, Radiation damage effects in zirconia, J. Nucl. Mater. 274 (1999) 66–77, https://doi.org/10.1016/S0022-3115(99)00041-0.

[14] V. Ponnilavan, M. Mushtaq Alam, M. Ezhilan, Kalpana Pandian, S. Kannan, Structural, mechanical, morphological and optical imaging characteristics of Yb3+ substituted zirconia toughened alumina, Mater. Today Commun. 24 (2020) 100983, https://doi.org/10.1016/j.mtcomm.2020.100983.

[15] K. Smits, L. Grigorjeva, D. Millers, A. Sarakovskis, J. Grabis, W. Lojkowski, Intrinsic defect related luminescence in ZrO2, J. Lumin. 131 (2011) 2058–2062, https://doi.org/10.1016/j.jlumin.2011.05.018.

[16] A. King, R. Singh, R. Anand, S.K. Behera, B.B. Nayak, Phase and luminescence behaviour of Ce-doped zirconia nanopowders for latent fingerprint visualisation, Optik 242 (2021) 167087, https://doi.org/10.1016/j.ijleo.2021.167087.

[17] Y. Hui, B. Zou, S. Liu, S. Zhao, J. Xu, Y. Zhao, X. Fan, X. Cao, Effects of Eu3+-doping and annealing on structure and fluorescence of zirconia phosphors, Ceram. Int., Part PB 41 (2015) 2760–2769, https://doi.org/10.1016/j.ceramint.2014.10.091.

[18] K. Kobayashi, H. Kuwajima, T. Masaki, Phase change and mechanical properties of ZrO2-Y2O3 solid electrolyte after ageing, Solid State Ionics 3–4 (1981) 489, https://doi.org/10.1016/0167-2738(81)90138-7.

[19] R. Di Monte, J. Kašpar, Nanostructured CeO2-ZrO2 mixed oxides, J. Mater. Chem. 15 (2005) 633, https://doi.org/10.1039/b414244f.

[20] D.H.A. Besisa, E.M.M. Ewais, Black zirconia composites with enhanced thermal, optical and mechanical performance for solar energy applications, Sol. Energy Mater. Sol. Cell. 225 (2021) 111063, https://doi.org/10.1016/j.solmat.2021.111063.

[21] E. Aleksanyan, M. Kirm, E. Feldbach, K. Kukli, S. Lange, I. Sildos, A. Tamm, Luminescence properties of Er3+ doped zirconia thin films and ZrO2/Er2O3 nanolaminates grown by atomic layer deposition, Opt. Mater. 74 (2017) 27–33, https://doi.org/10.1016/j.optmat.2017.05.003.

[22] S.V. Nikiforov, A.A. Menshenina, S.F. Konev, The influence of intrinsic and impurity defectsnon the luminescence properties of zirconia, J. Lumin. 212 (2019) 219, https://doi.org/10.1016/j.jlumin.2019.03.062.

[23] A. Sytchkova, M.L. Protopapa, P. Olivero, L. Tapfer, E. Burresi, T. Dunatov, Z. Siketic, M. Palmisano, E. Pesce, Y. Wang, Z. Wang, H. He, Optical characterization of the impact of 100 keV protons on the optical properties of ZrO2 films prepared by ALD on fused silica substrates, Appl. Opt. 62 (7) (2023), https://doi.org/10.1364/AO.487523C4. OIC1-OIC5.

[24] K. Smits, L. Grigorjeva, D. Millers, A. Sarakovskis, J. Grabis, W. Lojkowski, Intrinsic defect related luminescence in ZrO2, J. Lumin. 131 (2011) 2058, https://doi.org/10.1016/j.jlumin.2011.05.018.

[25] S.V. Nikiforov, A.A. Menshenina, S.F. Konev, The influence of intrinsic and impurity defectsnon the luminescence properties of zirconia, J. Lumin. 212 (2019) 219, https://doi.org/10.1016/j.jlumin.2019.03.062.

[26] T. Wang, G. Wang, M. Qiu, W. Cheng, J. Zhang, G. Zhao, The origin of the 500 nm luminescence band related to oxygen vacancies in ZrO2, J. Lumin. 237 (2021) 118133, https://doi.org/10.1016/j.jlumin.2021.118133.

[27] M. Rushton, I. Ipatova, L. Evitts, W. Lee, S. Middleburgh, Stoichiometry deviation in amorphous zirconium dioxide, RSC Adv. 9 (2019) 16320–16327, https://doi.org/10.1039/C9RA01865D.

[28] D. Islamov, V. Gritsenko, T. Perevalov, V. Aliev, V. Nadolinny, A. Chin, Oxygen Vacancies in Zirconium Oxide as the Blue Luminescence Centres and Traps Responsible for Charge Transport: Part II - Films, 2020, https://doi.org/10.2139/ssrn.3708728.

[29] M. Owen, M. Rushton, L. Evitts, A. Claisse, M. Puide, W. Lee, S. Middleburgh, Diffusion in doped and undoped amorphous zirconia, J. Nucl. Mater. (2021) 153108, https://doi.org/10.1016/j.jnucmat.2021.153108.

[30] A. Sytchkova, M.L. Protopapa, P. Olivero, E. Burresi, L. Tapfer, M. Palmisano, E. Pesce, T. Dunatov, Y. Wang, H. He, Optical characterization of the impact of 100 keV protons on the optical properties of ZrO2 films prepared by ALD on fused silica substrates, in: R. Sargent, A. Sytchkova (Eds.), Optical Interference Coatings Conference (OIC) 2022, Technical Digest Series, Optica Publishing Group, 2022, https://doi.org/10.1364/OIC.2022.WA.2 paper WA.2.

[31] D.A. Shirley, High-resolution X-ray photoemission spectrum of the valence bands of gold, Phys. Rev. B 5 (1972) 4709–4714, https://doi.org/10.1103/PhysRevB.5.4709.

[32] C. Henkel, S. Abermann, O. Bethge, E. Bertagnolli, "Atomic layer-deposited platinum in high-k/metal gate stacks", Semicond. Sci. Technol. 24 (2009) 125013.

[33] J.H. Scofield, Hartree-Slater subshell photo-ionisation cross-sections at 1254 and 1487eV, J. Electron. Spectrosc. Relat. Phenom. 8 (1976) 129–137, https://doi.org/10.1016/0368-2048(76)80015-1.

[34] J. Phys. Conf. 700 (2016) 012024, https://doi.org/10.1088/1742-6596/700/1/012024.

[35] P. Lackner, Z. Zou, S. Mayr, U. Diebold, M. Schmid, Using photoelectron spectroscopy to observe oxygen spillover to zirconia, Phys. Chem. Chem. Phys. 21 (2019) 17613, https://doi.org/10.1039/c9cp0.322j.

[36] S. Harel, J.-M. Mariot, C.F. Hague, Electronic structure at zirconia-nickel and zirconia-nickel oxide interfaces, Surf. Sci. 269 (270) (1992) 1167–1172, https://doi.org/10.1016/0039-6028(92)91411-4.

[37] P.C. Wong, Y.S. Li, K.A.R. Mitchell, XPS studies of the stability of a zirconium carbide film in the presence of zirconium oxide and hydrogen, Surf. Rev. Lett. 2 (3) (1995) 297–303, https://doi.org/10.1142/S0218625X95000315.

[38] C. Morant, J.M. Sanz, L. Galan, L. Soriano, F. Rueda, An XPS study of the interaction of oxygen with zirconium, Surface Science 218 (1989) 331–345, https://doi.org/10.1016/0039-6028(89)90156-8.

[39] D. Hauser, C. Grießer, E.-M. Wernig, T. Götsch, J. Bernardi, J. Kunze-Liebhäuser, S. Penner, The pervasive presence of oxygen in ZrC, Surface. Interfac. 34 (2022) 102373, https://doi.org/10.1016/j.surfin.2022.102373.

[40] G. Greczynski, L. Hultman, Reliable determination of chemical state in x-ray photoelectron spectroscopy based on sample-work-function referencing to adventitious carbon: resolving the myth of apparent constant binding energy of the C 1s peak, Appl. Surf. Sci. 451 (2018) 99–103, https://doi.org/10.1016/j.apsusc.2018.04.226.

[41] M.L. Protopapa, E. Burresi, M. Plamisano, E. Pesce, L. Latterini, N. Taurisano, G. Quaglia, R. Mazzaro, V. Morandi, Changing the microstructural and chemical properties of graphene oxide through a chemical route, Appl. Spectrosc. 76 (2022) 1452–1464, https://doi.org/10.1177/00037028221127048.

[42] J.F. Ziegler, J.P. Biersack, M.D. Ziegler, "SRIM – the Stopping and Range of Ions in Matter", Ion Implantation Press, Mormsville, NC, 2008.

[43] I. Di Sarcina, M.L. Grilli, F. Menchini, A. Piegari, S. Scaglione, A. Sytchkova, D. Zola, Behavior of optical thin-film materials and coatings under proton irradiation, Appl. Opt. 53 (2014) A314–A320, https://doi.org/10.1364/AO.53.00A314.

[44] Z. Wang, Y. Wang, H. He, A. Sytchkova, Z. Shen, M.L. Protopapa, Y. Zhang, C. Chen, Y. Chen, Y. Lu, M. Zhu, Y. Shao, J. Shao, Effect of residual impurities on the behavior and laser-induced damage of oxide coatings exposed to deep space radiation, Opt. Mater. 140 (2023) 113838, https://doi.org/10.1016/j.optmat.2023.113838.

[45] J. Sancho-Parramon, J. Ferré-Borrull, S. Bosch, A. Krasilnikova, J. Bulir "New calibration method for UV-vis photothermal deflection spectroscopy set-up" (Sytchkova), Appl. Surf. Sci. 256 (2006) 158–162, https://doi.org/10.1016/j.apsusc.2006.06.010.

[46] S. Logothetidis, Optical and electronic properties of amorphous carbon materials, Diam. Relat. Mater. 12 (2) (2003) 141–150, https://doi.org/10.1016/S0925-9635(03)00015-3.

[47] S.T. Barry, "Chemistry of Atomic Layer Deposition", Walter De Gruyter, Berlin-Boston, 2022 https://doi.org/10.1515/9783110712537.